Design, Analysis, and Implementation of Wireless Traveling-Wave Ultrasonic Motors

Zhiwei Xue, *Student Member, IEEE*, Kwok Tong Chau, *Fellow, IEEE*, Wei Liu, *Member, IEEE*, and Tze Wood Ching, *Senior Member, IEEE*

***Abstract*—Wireless motors have been extensively investigated for their flexibility and convenience, but they inevitably suffer from vulnerability to magnetic field interference, insufficient robustness, and the need for numerous power switches. Therefore, a wireless traveling-wave ultrasonic motor (USM) with high robustness is proposed in this paper, which artily integrates capacitive power transfer (CPT) into a USM to derive the brand-new non-magnetic wireless direct-drive motor. Prominently, differing from the existing wireless motors, the proposed wireless USM avoids the use of fragile microcontrollers and active or passive switches at the motor side, the control process of which can be completely conducted at the primary side, thus facilitating high-degree integration and maintenance-free operation. In addition, the bidirectional motion capability and flexible speed regulation can be readily achieved by changing the sequence and amplitude of two-phase outputs at the primary side, enabling the real sense of wireless direct drive. Finally, theoretical analysis and hardware experimentation are given to verify the feasibility of the proposed wireless USM for non-magnetic biomedical and aerospace applications.**

***Index Terms*—Ultrasonic motor, non-magnetic wireless motor, capacitive power transfer, high-robustness.**

I. INTRODUCTION

WIRELESS power transfer (WPT) is one of the most epoch-making technologies with obvious advantages such as high flexibility, reliability, low maintenance, and electrical isolation [1-4]. Compared with the cable power transmission method, WPT offers better flexibility, security, and mobility. Prominently, WPT has shown great application potential in the fields of biomedical devices [5], consumer electronics [6], induction heating [7] and electric vehicles [8, 9], which significantly facilitates the convenience of life.

Recently, the concept of wireless motors has been newly proposed and widely studied [10, 11]. Unlike conventional wired motors, WPT is utilized to wirelessly power the motors, which can effectively avoid wire wear and facilitate motor operation in harsh environments [12]. However, since both the primary and secondary sides are equipped with power devices and microcontrollers, the complexity and maintenance requirements inevitably increase. Therefore, developing wireless motors without any microcontroller and power device at the motor side is highly desirable.

Recently, wireless DC motors [13, 14], wireless AC induction motors [15], and wireless switched reluctance motors (SRMs) [16] have been proposed as more flexible and convenient alternatives to conventional wired motors [17]. Typical system configurations of these three types of wireless motors are shown in Fig. 1. Wireless DC motors require active and passive power switches at the motor side for bi-directional motion capability as shown in Fig. 1(a), which presents maintenance issues due to carbon brushes and commutators. On the other hand, wireless shaded-pole induction motors (SPIMs) require complex peripheral circuits such as multiple rectifiers and inverters as shown in Fig. 1(b), which reduces the overall system reliability and robustness. Moreover, bidirectional motion capability cannot be realized in this system. Although the wireless SPIM with dual stator windings and half-bridge inverters involves fewer power switches, the dual-stator SPIM requires special customization, thus increasing the system cost [18]. A multi-frequency wireless SRM has also been developed using selective WPT technology and multiple rectifiers as shown in Fig. 1(c), but it suffers from multi-frequency interference, delay, and vulnerability of Bluetooth.

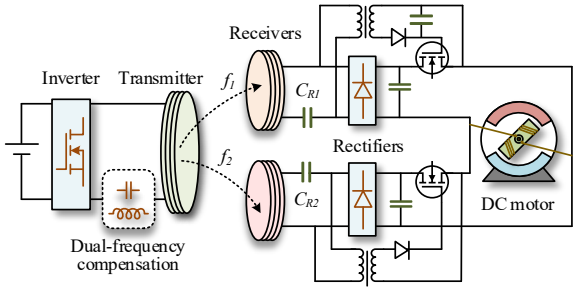

(a)

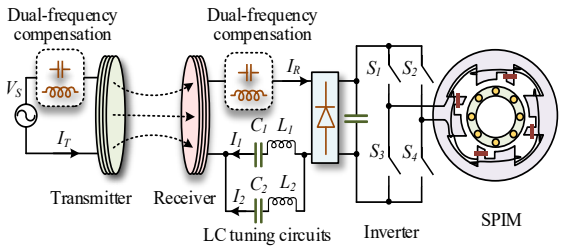

Manuscript received 04 June 2023; revised 27 September 2023; revised 22 November 2023; accepted 02 January 2024. This work was partially supported by a grant from the Hong Kong Research Grants Council, Hong Kong Special Administrative Region, China, under Project No. T23-701/20-R, and partially supported by a grant from The Hong Kong Polytechnic University, under Project No. P0048560. (Corresponding author: *K.T. Chau*.)

Zhiwei Xue and Tze Wood Ching are with the Department of Electrical and Electronic Engineering, The University of Hong Kong, Hong Kong, China. (e-mail: zwxue@eee.hku.hk; twching@eee.hku.hk).

Kwok Tong Chau and Wei Liu are with the Research Centre for Electric Vehicles and Department of Electrical and Electronic Engineering, The Hong Kong Polytechnic University, Hong Kong, China. (e-mail: k.t.chau@polyu.edu.hk; wei.liu@polyu.edu.hk).

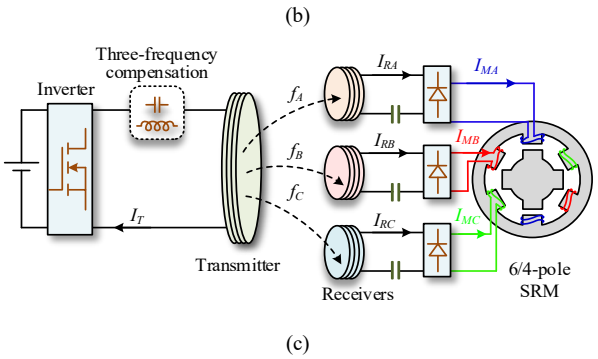

Fig. 1. System configurations of three types of wireless motors. (a) Wireless DC motor system with bi-directional motion capability [13]. (b) Wireless SPIM system [15]. (c) Multi-frequency wireless SRM system [16].

Although many efforts have been made to implement wireless motors, the real sense of the wireless direct drive cannot be realized as they all require power switches or communication devices at the motor side, which negatively affects the reliability and maintainability of the system. Moreover, the misalignment of coupling mechanisms compromises the robustness of the system, limiting their practical applications. Meanwhile, the above-mentioned wireless motors are developed based on inductive power transfer (IPT) [19], in which the high-frequency magnetic fields are prone to eddy current losses, resulting in heating effects. They are also susceptible to electromagnetic interference (EMI) [20, 21]. In addition, the coupling mechanism occupies ample space with heavyweight, which is not conducive to promoting lightweight and integration.

Capacitive power transfer (CPT) utilizes electric fields to achieve wireless power transfer and offers the advantages of lightweight, high design flexibility and low cost compared with IPT systems [22]. In practical applications, wireless charging of special loads such as batteries requires load-independent constant-current (CC) or constant-voltage (CV) outputs to suit different requirements. The two-sided LCL [23] and LCLC [24] compensation networks have CC output and zero phase angle characteristics. As for CV output, topologies such as LCL-L [25] and LCL [26] can be easily realized. Meanwhile, some topologies such as bilateral LC can realize both CC and CV outputs [27]. On the other hand, the pole plate voltage stress is also a concern for CPT systems as excessive voltage can cause breakdown problems. A two-stage parametric design methodology is proposed in [28] to minimize the reactive power flow and the pole plate voltage stress. In [29], a system circuit design methodology based on degrees of freedom is proposed to minimize the coupler voltages.

To address the aforementioned issues, a brand-new non-magnetic wireless ultrasonic motor (USM) system is proposed and implemented in this paper, which offers distinct advantages of real-sense of wireless direct drive without any power switches and communication equipment at the motor side. More importantly, the insensitivity to the misalignment of the coupling mechanism makes the proposed system more advantageous over other wireless motors in practical applications. The specific contributions and improvements of the proposed wireless USM are summarized as follows:

(1) The real-sense of wireless direct drive can be readily achieved without using microcontrollers and active or passive power switches at the motor side, facilitating a fully sealed design with high robustness and maintenance-free operation.

(2) The proposed system can overcome the shortcomings of IPT-based wireless motors in terms of sensibility to coupling mechanism misalignment. It maintains high robustness even in the case of coupling capacitance variation.

(3) The operation of the proposed system does not rely on electromagnetic principles, making it well-suited for biomedical and aerospace applications.

(4) Flexible speed regulation and bidirectional motion control can be easily realized at the primary side without complex peripheral circuitry.

II. Configuration of Proposed Wireless USM

As a non-magnetic WPT method, CPT is perfect for wirelessly powering the USM. Different from the IPT system, the CPT system takes definite advantage of the high-frequency electric field to achieve WPT with low electromagnetic interference and low eddy current loss.

A general configuration of the proposed wireless USM is shown in Fig. 2, which mainly comprises three parts, namely, the full-bridge inverters, 2-phase LC-CLC compensated CPT networks and a USM. The full-bridge inverters are utilized as the high-frequency AC power source to supply power to the transmitter plates after the primary LC-compensated network. Then, the displacement current will be induced by the alternating electric field between the transmitter and receiver plates, enabling contactless power transfer. The receiver side utilizes the CLC-compensated network to convert the received power into the appropriate voltage required by the USM. Since the USM is inherently capacitive, two inductors are purposely connected in series at the input terminals of the USM to resonate with the inherent parasitic capacitance. The proposed wireless USM system is driven simultaneously by two independent CPT systems with the same output voltage amplitude and a phase difference of 90 degrees. In this way, traveling waves can be generated in the stator to drive the motor wirelessly. Meanwhile, motor commutation control can be performed entirely at the primary side by simply changing the 90-degree phase angle difference to −90 degrees. The specific details will be introduced in the hereinafter.

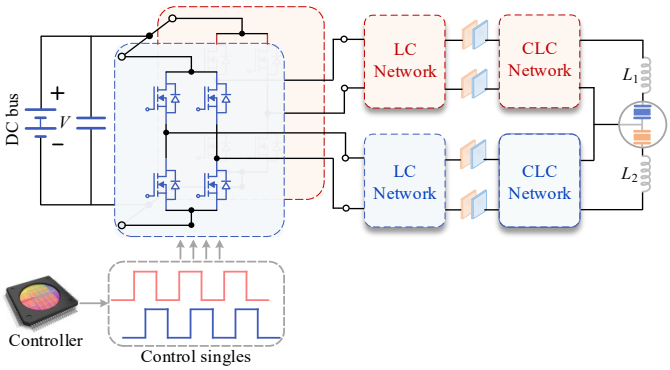

Fig. 2. Configuration of proposed wireless USM.

III. Structure and Working Principles of USM

The USM utilized in this paper is the Shinsei USR60, its typical structure is shown in Fig. 3. The stator consists of piezoelectric elements and elastomers. The rotor is made of bronze and is kept in pressure contact with the stator under the action of preload [30]. The contact surface between the rotor and stator is coated with a layer of special friction material, which is a blend of 30% Ekonol in 70% Polytetrafluoroethylene with a friction coefficient of 0.20 to increase the friction between the bronze and the elastomer.

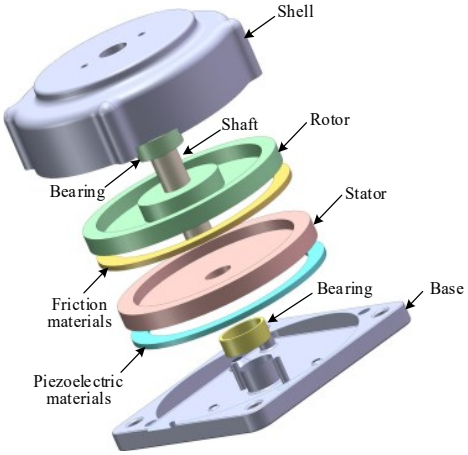

Fig. 3. Typical structure of USM.

The stator is bonded with two piezoelectric ceramic arrays A and B, each consisting of eight alternately polarized segments of width λ/2 (λ is the wavelength), with an offset between the two arrays of λ/4 [31]. Specifically, when two-phase sinusoidal waves with a phase shift of 90° are applied to the two-phase piezoelectric elements, two orthogonal standing waves with the same frequency can be generated, which can be superimposed on the stator and coupled into a traveling wave [32].

The single-phase standing wave excited on the A-phase piezoelectric element can be expressed as

$$W_A(x,t)=\xi_A\cos kx\cos\omega t \tag{1}$$

Similarly, the standing wave obtained via exciting the B-phase piezoelectric element can be given by

$$W_B(x,t)=\xi_B\cos kx'\cos(\omega t-\theta) \tag{2}$$

where ξ_A and ξ_B are the amplitudes of the radial vibration of phases A and B, respectively, k is the wave number of the elastic waves ($k = 2\pi/\lambda$, λ is the wavelength), x and x' are the space intervals of phases A and B, respectively, ω is the angular frequency of vibration, and θ is the phase difference between phases A and B [33]. According to the layout of the piezoelectric elements, it yields $x' = x-\lambda/4$. Due to the 90° phase shift in the two-phase voltage, $\theta = \pi/2$ is resulted. Therefore, the B-phase standing wave equation can be deduced as

$$W_B(x,t)=\xi_B\sin kx\sin\omega t \tag{3}$$

Accordingly, when the two-phase piezoelectric elements are symmetrically polarized, namely, $\xi_A=\xi_B=\xi_0$, the superposition of the two-phase standing wave can be obtained as

$$W(x,t)=W_A(x,t)+W_B(x,t)=\xi_0\cos(kx-\omega t) \tag{4}$$

Similarly, when $\theta = -\pi/2$, the superposition of the two standing waves can be given by

$$W(x,t)=W_A(x,t)+W_B(x,t)=\xi_0\cos(kx+\omega t) \tag{5}$$

According to (4) and (5), the two-phase sinusoidal voltages with the same amplitude, same frequency and 90° phase difference can excite two-phase standing waves with π/2 space and time differences on the piezoelectric elements. The two orthogonal standing waves superimposed on the stator form a continuous traveling wave, thereby generating rotational motion through friction between the stator and the rotor. In addition, by altering the phase difference between phases A and B, the direction of the traveling wave can be reversed, and the bidirectional motion of the motor can be achieved [34].

On the other hand, the motor speed increases linearly with the amplitude of the traveling wave, which is positively correlated with the vibration amplitude of the piezoelectric material. Therefore, flexible speed regulation can be achieved by adjusting the terminal voltage according to the characteristics of the vibration amplitude of the piezoelectric material and terminal voltages. It is worth noting that at low driving terminal voltages, the vibration amplitude of the piezoelectric material is small, and the friction between the stator and the rotor is insufficient to overcome the preload force to drive the motor, resulting in the motor being in a static state.

IV. System Design and Analysis

The control characteristics of USM are complex and highly nonlinear due to its equivalent impedance value varying with the rotation direction, rotor speed, and friction between the stator and rotor. Considering that USMs are voltage-driven motors, the constant input voltage of the motor terminal is critical to ensuring their stable operation. Therefore, a load-independent LC-CLC compensated CPT system with constant output voltage characteristics is designed and analyzed to ensure stable control performance of the proposed wireless USM even under time-varying parameter conditions.

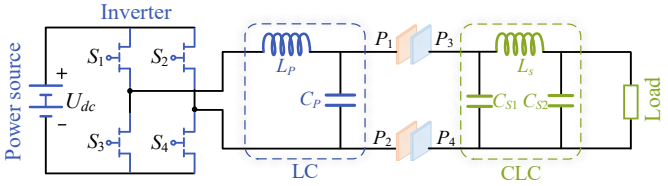

Fig. 4. System structure of LC-CLC compensated CPT.

As shown in Fig. 4, the proposed LC-CLC compensated CPT system consists of the DC voltage source, full-bridge inverter, primary side LC-compensated network composed of L_P and C_P, coupled metal plates composed of P_1-P_4, secondary side CLC-compensated network composed of C_{S1}, L_S and C_{S2}, and a load.

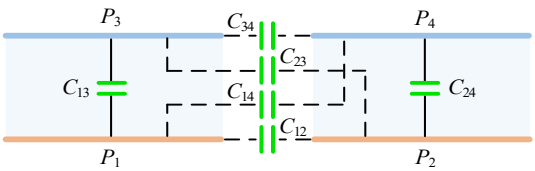

Fig. 5. Circuit model of capacitive coupler.

It can be seen from Fig. 5 that the coupling mechanism is composed of four aluminum plates, P_1-P_4. The aluminum plates P_1 and P_2 are placed at the primary side as the transmitter plates, while the aluminum plates P_3 and P_4 are placed at the secondary side as the receiver plates. It is worth noting that the mutual capacitance will be induced between two different aluminum plates and a total of 6 equivalent capacitances will be induced among P_1-P_4, as shown in Fig. 5. In the proposed system, water is added between the pole plates to increase the coupling capacitance, which is stored in polyethylene bags and placed in acrylic containers to ensure that there will be no conductive power transmission problems. In addition, solid mediums such as FR-4 can also be used instead of liquid mediums, which can provide better flexibility and do not require special seals. As a result, the coupling capacitances C_{12} and C_{34} and the cross-coupling capacitances C_{14} and C_{23} are much smaller than C_{13} and C_{24} [35]. Therefore, the four coupling capacitances can be ignored and the system can be simplified as shown in Fig. 6.

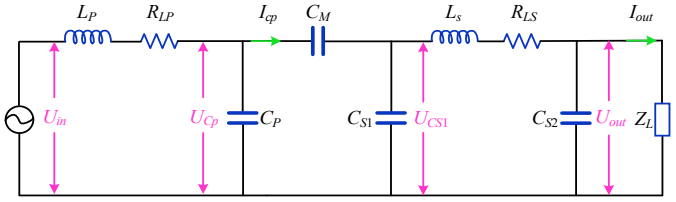

Fig. 6. Simplified equivalent circuit of LC-CLC compensated CPT.

The root mean square (RMS) value of the output voltage of the inverter can be equal to a constant voltage source U_{in}, which can be calculated as

$$U_{in} = \frac{2\sqrt{2}}{\pi} U_{dc} \tag{6}$$

where U_{dc} is the DC bus voltage. Meanwhile, the coupling capacitance C_{13} and C_{24} can be represented by the equivalent series coupling capacitance C_M as given by

$$C_M = \frac{C_{13}C_{24}}{C_{13}+C_{24}} \tag{7}$$

A. Primary LC-Compensated Network

The LC-compensated network at the primary side is composed of L_P and C_P, which can effectively suppress the harmonic output of the inverter and boost its output voltage to stimulate the transmitter plate. When Z_e is the equivalent impedance after the primary LC-compensated network, the equivalent circuit of the system can be simplified as depicted in Fig. 7(a). For the sake of simplicity, the equivalent resistance of the compensation capacitors can be neglected since they have little effect on the system efficiency. Then, according to Norton's theorem [36], the primary circuit shown in Fig. 7(a) can be represented by a Norton circuit, as shown in Fig. 7(b).

Based on the circuit equivalence principle, the input current of the Norton equivalent circuit can be expressed as

$$\dot{I}_{in} = \frac{\dot{U}_{in}}{R_{Lp} + j\omega L_p} \tag{8}$$

The admittance Y_p of the parallel LC network shown in Fig. 9(b) can be expressed as

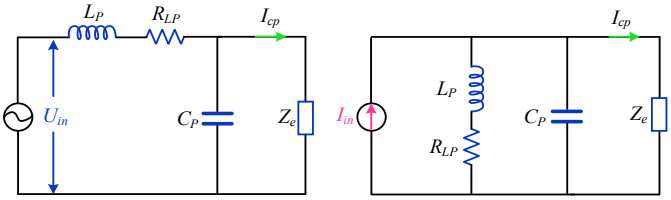

(a) (b)

Fig. 7. Equivalent circuit of primary LC-compensated network. (a) Primary circuit. (b) Norton equivalent circuit.

$$\begin{aligned} Y_p &= \frac{1}{R_{Lp} + j\omega L_p} + j\omega C_p \\ &= \frac{R_{Lp}}{R_{Lp}^2 + \left(\omega L_p\right)^2} + j\omega\left(C_p - \frac{L_p}{R_{Lp}^2 + \left(\omega L_p\right)^2}\right) \end{aligned} \tag{9}$$

For constant operating frequency f and compensating inductance L_p, the admittance Y_p of the parallel LC network can be minimized when the imaginary part is zero. Hence, it yields

$$C_p - \frac{L_p}{R_{Lp}^2 + \left(\omega L_p\right)^2} = 0 \tag{10}$$

Then, the compensation capacitor C_p can be deduced as

$$C_p = \frac{L_p}{R_{Lp}^2 + \left(\omega L_p\right)^2} \tag{11}$$

The output current I_{cp} of the Norton equivalent circuit can be deduced as

$$\dot{I}_{cp} = \dot{I}_{in}\frac{Z_p}{Z_p + Z_e} \tag{12}$$

where Z_p is the impedance of the parallel LC network.

When the admittance Y_p of the parallel LC network is smaller, the larger its equivalent impedance Z_p is. Therefore, it is necessary to ensure that the internal resistance of the primary compensation inductor can meet the following conditions

$$R_{Lp} \ll \omega L_p \tag{13}$$

Accordingly, the compensation capacitor C_p can be further simplified as

$$C_p = \frac{1}{\omega^2 L_p} \tag{14}$$

In this case, the admittance Y_p of the parallel LC network is minimum, namely, its impedance Z_p is maximum and much larger than Z_e. Therefore, the output current I_{cp} of the Norton circuit is closer to the input current I_{in} which can be expressed as

$$\dot{I}_{cp} \approx \dot{I}_{in}\frac{Z_p}{Z_p} \approx \frac{\dot{U}_{in}}{j\omega L_p} \tag{15}$$

According to the above analysis, the primary LC network can supply an approximately constant current to the rear circuit independent of the coupling capacitance, which means the variation of coupling capacitance will not affect the constant current input to the secondary circuit, thus ensuring robustness to the coupling mechanism misalignment.

B. Secondary CLC-Compensated Network

As aforementioned, the primary circuit of the CPT system can be approximately regarded as a constant current source under certain conditions. Similarly, the secondary circuit can be simplified as shown in Fig. 8(a). According to the principle of circuit equivalence, the circuit shown in Fig. 8(a) can be represented by a Thevenin circuit as depicted in Fig. 8(b). Then, the equivalent voltage source can be expressed as

$$\dot{U}_s = \frac{Z_{C_{S1}} Z_{C_{S2}}}{Z_{C_{S1}} + Z_{L_s} + Z_{C_{S2}}} \dot{I}_{cp} \tag{16}$$

where Z_{CS1}, Z_{Ls} and Z_{CS2} are the impedance of capacitance C_{s1}, inductance L_s, and capacitance C_{s2} in the secondary CLC-compensated network, respectively. Meanwhile, the equivalent impedance Z_s in Fig. 8(b) can be derived as

$$Z_s = \frac{Z_{C_{S2}} \left(Z_{C_{S1}} + Z_{L_s} \right)}{Z_{C_{S1}} + Z_{L_s} + Z_{C_{S2}}} \tag{17}$$

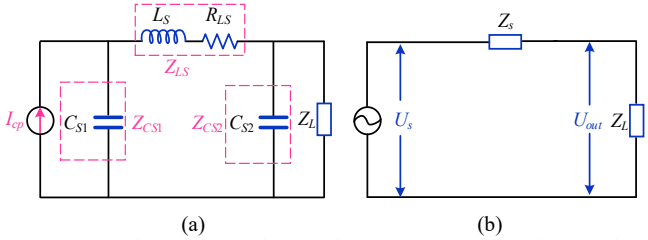

Fig. 8. Equivalent circuit of secondary CLC-compensated network. (a) Equivalent circuit of secondary side. (b) Equivalent Thevenin circuit.

According to Kirchhoff's voltage law, the smaller the impedance Z_s, the closer the output voltage is to the input voltage. Specifically, the inductor L_s should be fully compensated by the capacitor C_{s1} at the resonant frequency. As a result, the impedance Z_s can be simplified as

$$Z_s = \frac{Z_{C_{S2}} R_{L_s}}{R_{L_s} + Z_{C_{S2}}} \tag{18}$$

where R_{Ls} is the internal resistance of inductor L_s.

To simplify the calculation, the resistance R_{Ls} can be ignored since it is much smaller than the equivalent impedance of C_{s2}. Then (18) can be simplified as

$$Z_s = R_{L_s} \tag{19}$$

Accordingly, the output voltage U_{out} can be expressed as

$$\dot{U}_{out} = \frac{Z_L}{R_{L_s} + Z_L} \dot{U}_s \tag{20}$$

Since the impedance of USM is much larger than R_{Ls}, the output voltage can be further simplified as

$$\dot{U}_{out} \approx \dot{U}_s \approx Z_{C_{S1}} \dot{I}_{cp} \tag{21}$$

Based on (21), the output voltage of the secondary compensated network is approximately constant under certain conditions, which is only dependent on the input current I_{cp} and the impedance Z_{CS1}.

C. System Flexibility and Output Characteristics

In order to further illustrate the flexibility of the CPT system, the constant output voltage characteristics are investigated. As aforementioned, when the system parameters meet certain conditions, the system output voltage can be expressed as

$$\dot{U}_{out} = Z_{C_{S1}} \dot{I}_{cp} = \frac{Z_{C_{S1}} \dot{U}_{in}}{j\omega L_p} \tag{22}$$

In general, as $1/j\omega C_{S1}$ is much larger than its equivalent resistance, the output voltage can be simplified as

$$\dot{U}_{out} \approx -\frac{\dot{U}_{in}}{\omega^2 L_p C_{S1}} \tag{23}$$

The ratio of compensation inductor L_s to L_p is defined as k, $k = L_s/L_p$. When the resonant frequency of the primary LC-compensated network and the secondary CLC-compensated network are the same, namely $\omega^2 L_p C_p = \omega^2 L_s C_{s1} = 1$, (23) can be deduced as

$$\dot{U}_{out} = -\frac{\dot{U}_{in}}{\omega^2 L_p C_{S1}} = -\frac{L_s \dot{U}_{in}}{L_p} = -k\dot{U}_{in} \tag{24}$$

As shown in (24), when the system parameter configuration meets the qualified and resonant conditions, the output voltage only depends on the input voltage U_{in} and the inductor ratio k. The output voltage is k times the input voltage with the opposite phase. Therefore, the performance of wireless USM cannot be affected by the variation of coupling capacitance and load within a certain degree.

V. System Analysis

Since the 40 kHz resonant frequency is relatively low for a typical CPT system, detailed simulations are performed to analyze the effects of the designed CPT system in terms of the transmission power and voltage stress when driving the USM.

A. Transmission Power Analysis

In order to analyze the power transfer performance of the designed CPT system, Fig. 9 shows the transmission power with different input voltages. It can be seen that the transmission power increases gradually with the increase of the input voltage since the designed CPT topology has a constant voltage output characteristic that is proportional to the input voltage. The analysis results show that the 40 kHz CPT system is suitable for low-power applications. Considering that the power level of USM is generally low, the low-frequency CPT can satisfy the transmission power requirements of USM.

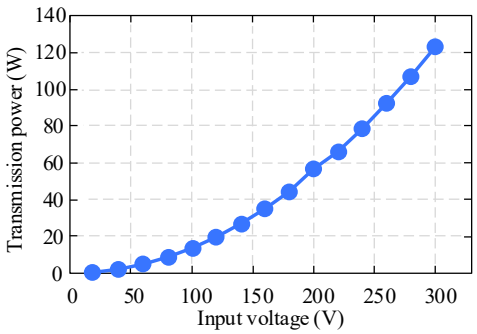

Fig. 9. Transmission power of designed CPT with different input voltages.

B. Pole-Plate Voltage Stress Analysis

In order to analyze the pole-plate voltage stress of the designed CPT system, Fig. 10 shows the voltage stress with different output power levels. Specifically, the voltage stress increases with the increase of the output power. However, it is noteworthy that the voltage stress always remains at a relatively low level, ensuring that the system does not encounter issues such as sparking or breakdown. In addition, to ensure the safety of human exposure to electric fields, the electric field distribution on the plate is evaluated by Finite Element Analysis as shown in Fig. 11. According to the IEEE standard [37], the electric field strength of 28 mm away from the pole plate is safe for human safety at 40 kHz electric field.

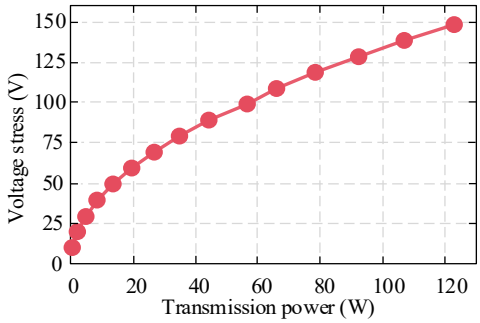

Fig. 10. Pole-plate voltage stress of designed CPT with different output power.

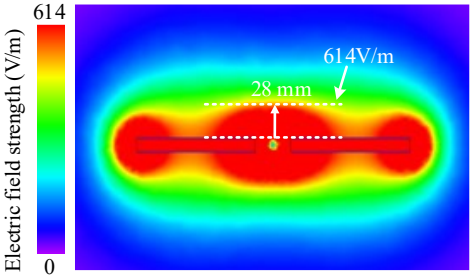

Fig. 11. Electric field distribution on the plate.

VI. Implementation and Experimental Verification

To verify the feasibility of the proposed system, a practical prototype is constructed, and a test setup is established, as shown in Fig. 12. Specifically, the voltage and current are measured with probes (LeCroy ADP300) and (LeCroy CP030), respectively, and recorded by an oscilloscope (LeCroy 6100A). The control program is realized by the digital signal processor (DSP) microcontroller (TMS320F28335), and the DC power supply (Ametek DLM300-10E) is used to power the gallium nitride (GaN) full-bridge inverters. Due to the low resonant frequency of the designed CPT system, the amount of compensation inductance will be relatively large. To solve this problem, the compensation inductors L_p and L_s are wound with Leeds wire, and two ferrite bars are mounted inside the coil, thus greatly reducing the coil size and internal resistance. The compensation capacitors are composed of polypropylene film capacitors. The design specifications are listed in Table I.

TABLE I
DESIGN SPECIFICATIONS AND PARAMETERS

Items	Value/type
Resonant frequency (f)	40 kHz
LC-compensated inductance (L_{pa}, L_{pb})	16.70, 16.73 mH
LC-compensated capacitance (C_{pa}, C_{pb})	951.4, 950.7 pF
Resistance of primary inductor (R_{pa}, R_{pb})	1.8, 1.8 Ω
CLC-compensated inductance (L_{sa}, L_{sb})	8.69, 8.78 mH
CLC-compensated capacitance (C_{sa1}/C_{sa2}, C_{sb1}/C_{sb2})	1.82/1.81, 1.82/1.82 nF
Resistance of secondary inductor (R_{sa}, R_{sb})	1.4, 1.4 Ω
Capacitance of coupling mechanism (C_M)	1271 pF
Aluminum plate size (S)	100×100×1 mm^3
Compensated inductance size (S_i)	90×30×25 mm^3
Series inductors (L_1, L_2)	1.0, 1.0 mH
GaN inverter (full-bridge)	GS66508B
USM rated voltage	130 V
USM rated Torque	50 Ncm

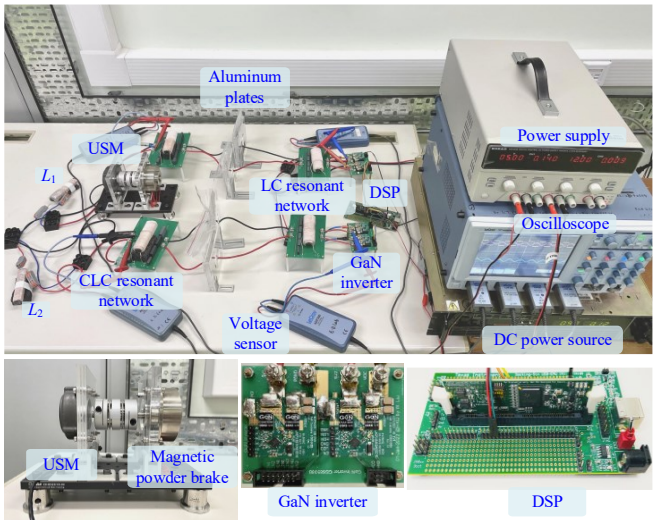

Fig. 12. Experimental setup.

Fig. 13(a) shows the measured waveforms of the two-phase output voltages of the primary-side LC-compensated networks u_{pa}/u_{pb}, and the input voltage of the motor terminals u_{ta}/u_{tb}. Specifically, the primary-side LC-compensated network can effectively suppress the high-order harmonic contents of the inverter and boost the amplitude of the output voltage to stimulate the transmitter plate for WPT. The input voltage of phase A is 90° ahead of phase B, which can excite two standing waves on the stator of USM, respectively. Then, a traveling wave will be generated by the superposition of the two standing waves to drive the rotor rotating clockwise (CW). Additionally, the motion of the USM in the opposite direction is evaluated as shown in Fig. 13(b). When the phase difference between the terminal voltages of phase A and phase B changes from 90° to −90°, namely, phase B is 90° ahead of phase A, the traveling wave formed by the superposition of the two standing waves will change its traveling direction and the rotor will rotate counterclockwise (CCW). Therefore, by changing the phase difference of the two-phase terminal voltages of USM, the bidirectional motion of USM can be flexibly realized.

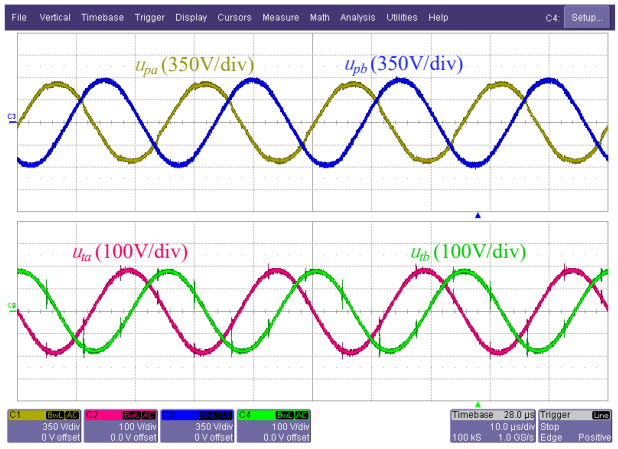

(a)

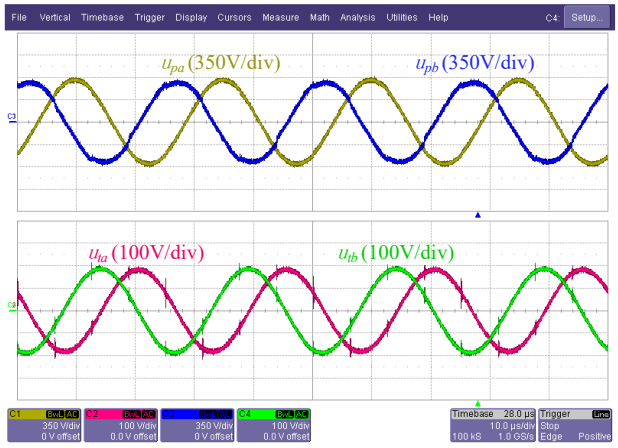

(b)

Fig. 13. Measured waveforms of proposed wireless USM. (a) CW rotation. (b) CCW rotation.

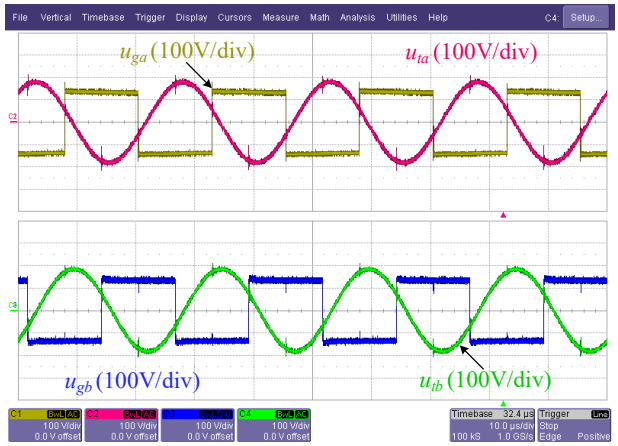

Fig. 14. Measured waveforms of output voltages of inverter and terminal voltage of USM.

Fig. 14 shows the measured waveforms of the output voltage of the full-bridge inverters u_{ga}/u_{gb} and the terminal voltages of the motor u_{ta}/u_{tb}. The full-bridge inverters output two-phase square wave voltages with a phase difference of 90° at the switching frequency of 40 kHz. After the LC-CLC compensated CPT system, two alternating currents with a phase difference of 90° are inputted to the terminals of USM. Therefore, the bidirectional motion of wireless USM can be easily achieved by programming the microcontroller at the primary side, without involving any controllers and active or passive switches at the motor side.

To further assess the bidirectional motion characteristics of the wireless USM, the bidirectional speed responses versus the terminal voltage are measured as shown in Fig. 15. It can be observed that with the rated voltage of 130 V, the rotor speed can reach up to 169 rpm. In particular, the motor speed increases linearly with the increase of the terminal voltage within a specific range. This is because changing the amplitude of the terminal voltage of USM can adjust the amplitude of the traveling wave generated on the stator surface, thus realizing flexible speed regulation of USM. In addition, at low drive voltages, the amplitude of the traveling wave decreases and therefore friction cannot overcome the preload to drive the motor. The characterization between voltage and vibration response amplitude of the piezoelectric ceramics can be referenced from [38] for a better understanding of the relationship between the drive voltage and motor speed.

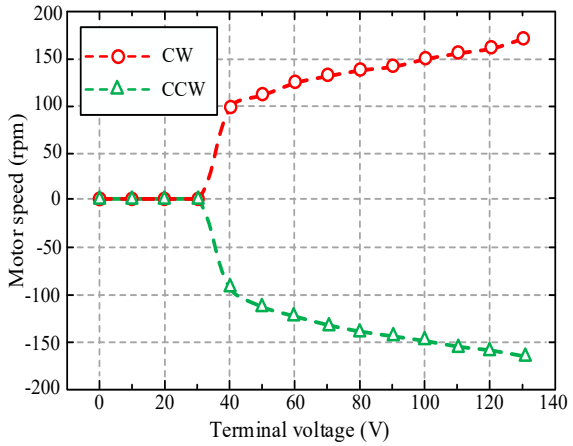

Fig. 15. Measured bidirectional speed characteristics of wireless USM.

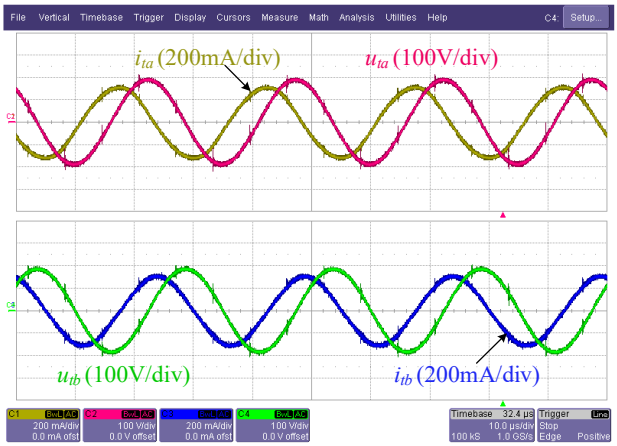

Fig. 16. Measured waveforms of current and voltage of wireless USM.

Furthermore, Fig. 16 demonstrates the measured waveforms of motor terminal voltages u_{ta}/u_{tb} and currents i_{ta}/i_{tb} with the load torque of 25 Ncm. Under the rated terminal voltage, the RMS value of stator current is 0.22 A. In addition, the stator current leads the voltage because of the capacitive load characteristics of the USM. Moreover, Fig. 17 shows the measured speed characteristics of USM with a load of 10 Ncm and 25 Ncm, respectively. It can be seen that the motor speed

can be controlled from 77 to 163 rpm at 10 Ncm load and 69 to 150 rpm at 25 Ncm load, respectively. In particular, the motor speed decreases linearly as the load torque increases, which is similar to the wired USM system. Therefore, these measured results well verify the feasibility of the proposed wireless USM.

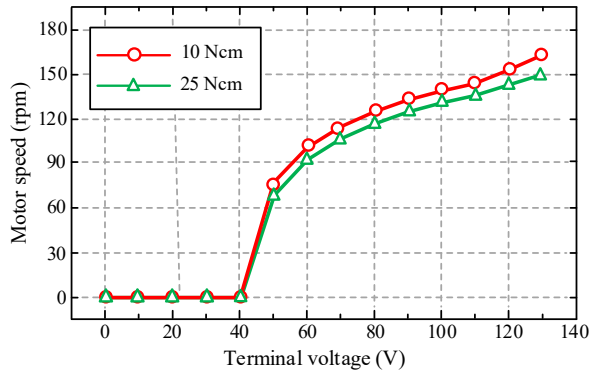

Fig. 17. Measured speed characteristics against motor terminal voltage.

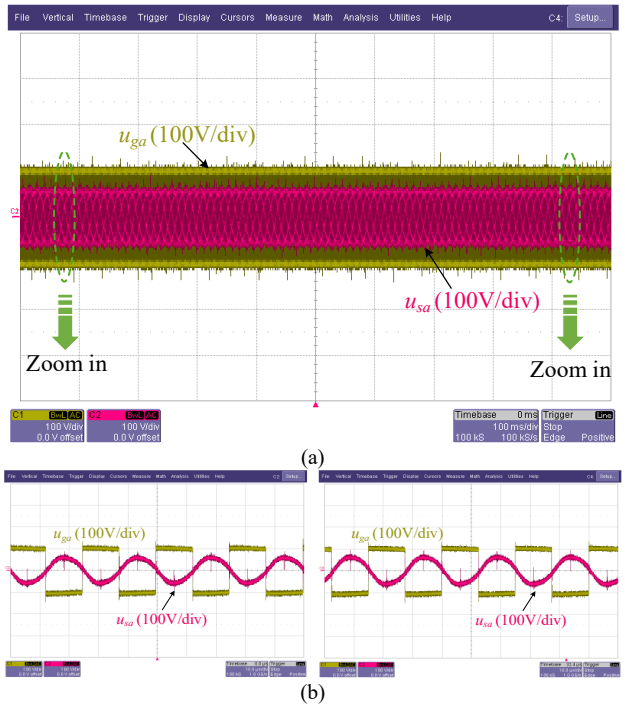

Fig. 18. Measured waveforms of input and output voltages of CPT. (a) Full view. (b) Zoom-in view with no load (left) and load of 10 Ncm (right).

The constant voltage output characteristics of the CPT system are assessed experimentally. Fig. 18 shows the measured waveforms and their zoom-in ones under load variation, including the output voltage of the inverter u_{ga}/u_{gb} and the output voltage of the secondary CLC-compensated network u_{sa}/u_{sb}. It can be observed that the output voltage is basically constant when the load is changed from 0 Ncm to 10 Ncm. The zoom-in waveforms provide more detailed information. Before and after the motor load changes, the output voltage of the system is always maintained between 43.0–43.7V, showing good constant-voltage output characteristics. In addition, the RMS value of the input voltage is 90 V, and the gain of output and the input voltage is about 0.48 with a phase difference of 180° between them. Considering the impedance of the system, the ratio of the input and output voltages can match with L_{sa}/L_{pa} within an acceptable range. Therefore, the constant output voltage characteristic and flexible output voltage gain design of the CPT system guarantees the feasibility of the wireless direct drive of USM.

Then, the robustness of the proposed wireless USM with respect to the coupling capacitance of the coupling mechanisms is investigated as shown in Fig. 19. It can be observed that when the coupling capacitance is varied in a wide range, the motor speed remains stable at around 120 rpm during steady-state operation. Therefore, the experimental results indicate that the proposed wireless USM system is insensitive to the misalignment of the coupling mechanism, ensuring reliable performance under diverse operating conditions, thereby highlighting its robustness in the face of potential misalignment issues associated with the coupling mechanism.

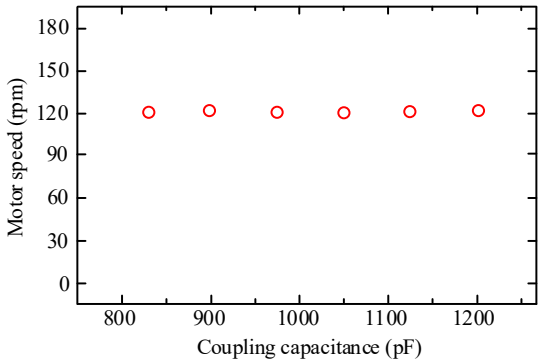

Fig. 19. Measured motor speed varies with coupling capacitance.

Finally, the system efficiency, output power and power loss distribution of the CPT system are evaluated as shown in Fig. 20. In the case of forward and backward motions, the efficiency is basically the same, up to 75.17% and 74.2%, respectively. In the power loss test, although the amount of inductance is large, the power loss is relatively small due to the low current flow in the system. In addition, the inverter loss accounts for a large proportion. Considering the low power level of USMs, the application of a half-bridge inverter will help to further improve the efficiency. Moreover, the optimization of the compensation network and the coupling mechanism is crucial for improving transmission efficiency.

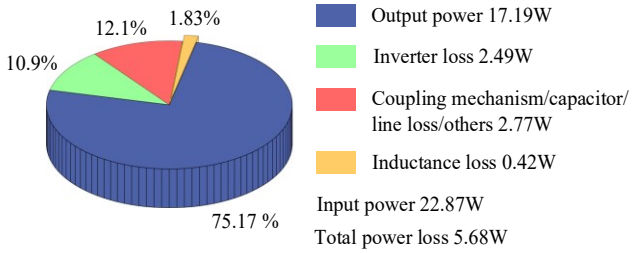

Fig. 20. Output power and loss distribution of CPT system.

VII. Discussion and Recommendation

To highlight the uniqueness of the proposed wireless USM system, a quantitative comparison with reported wireless motor systems is presented in Table II. All of them utilize more than a dozen power switches at the motor side, resulting in increased complexity and concerns regarding system stability. In addition, multi-frequency WPT is widely employed for selective feeding of motor windings, which inevitably introduces multi-frequency crosstalk and EMI noise into the system.

In contrast, the proposed non-magnetic wireless USM system utilizes zero power switches (both active and passive) and zero communication modules as well as only single-frequency WPT to directly drive the motor, which offers significant advantages in terms of high integration, reliability, and simplicity. More importantly, the proposed system also exhibits superior performance in terms of sensitivity to coupling mechanism misalignment. Specifically, variations in the coupling capacitance have limited influence on the control system, thus greatly enhancing the robustness of the whole system. In addition, since both CPT and USMs operate independently of electromagnetic principles, the proposed system has considerable potential for application in biomedical and aerospace fields.

In terms of the practical applications, the sealing of the medium (like water) in the coupling mechanism and the possibility of the presence of conductive power transfer need to be considered. In this work, polyethylene bags are used to store the medium water, thus cutting off the possibility of conductive power transfer while achieving the physical sealing. In addition, it is recommended to use USMs with higher drive frequency, which will reduce the amount of inductance used in the CPT system and facilitate further integration.

On the other hand, due to the duality of IPT and CPT systems, IPT is also applicable to this study, and the amount of inductance used is smaller than that of the CPT system under the 40 kHz frequency. However, as the resonant frequency of the ultrasonic motor increases, the volume of the CPT compensation inductors will be reduced. In addition, the proposed CPT system does not require special designs of the capacitive coupling mechanism, the typical two-pair plate structure can realize constant voltage output independent of the coupling capacitance, which provides high system robustness. In contrast, IPT systems usually require special designs of the inductive coupling mechanism to reduce the sensitivity to misalignment [39], which is complex and cumbersome. Therefore, the proposed CPT system can naturally achieve high robustness compared to IPT by simply using a conventional capacitive coupling structure.

As a non-magnetic wireless motor, the proposed wireless USM has great promise in strong magnetic environments and medical implants. In the field of magnetic resonance imaging (MRI)-guided robots, it can be integrated into robotic systems used in MRI environments, allowing great potential for precise and controlled movement during procedures. The wireless power direct drive eliminates the need for physical connections, which can interfere with the imaging process and restrict the robot's range of motion. In addition, with its simple structure and flexible controllability, the proposed wireless USM offers wireless direct control without requiring invasive procedures to replace batteries, making it promising for application in medical implants such as pacemakers. This technology enables efficient and convenient power drive and control to the implanted device, improving patient comfort and reducing the risks associated with repeated surgeries. In addition, it is promising to address the nuisance of implanted patients who cannot be examined in strong magnetic environments such as MRI equipment.

For further research, as the receiver side of the proposed wireless motor system is already simplified enough (eliminating power switches, sensors, communication modules, and complex peripheral circuits to drive the power switches), the integration of receiver-side inductance is a promising research direction to promote further simplification of the wireless motor system. It is promising that the CPT systems have the potential for further integration. Specifically, the receiver-side compensation inductor of series-series (SS) CPT and parallel-series (PS) CPT structures can be connected in series with the filter inductor to form a single inductor, thus realizing the potential for further integration. In contrast, the potential for inductor integration in IPT systems remains to be developed.

TABLE II
Comparison of Existing Systems and Proposed System

Ref.	Resonant frequency	Compensation network	Bidirectional motion	Active switches	Passive switches	Communication modules	Robustness
[10]	100 kHz	S-S	√	0	12	1	Low
[13]	130, 160 kHz	LCL-S	√	2	10	0	Low
[15]	109, 116 kHz	LCL-LC	×	5	28	0	Low
[16]	91, 112, 137 kHz	S-S	√	0	12	1	Low
Proposed	40 kHz	LC-CLC	√	0	0	0	High

VIII. Conclusion

In this paper, the wireless USM has been proposed and implemented, which adopts the CPT to drive the USM directly, deriving the first non-magnetic wireless motor. This novel system is particularly advantageous for applications that are susceptible to strong magnetic environments, featuring maintenance-free operation and high-robustness. Notably, unlike previous wireless motors, the obvious merits of the proposed wireless USM are that no power switches, microcontrollers and communication devices are configured at the motor side, and the flexible speed regulation and bidirectional motion can be performed entirely at the primary side, realizing the real sense of wireless direct drive.

Importantly, the proposed wireless USM overcomes a notable limitation of existing wireless motors that are sensitive to the misalignment of the coupling mechanism, thus paving the way for further practical application. Finally, an experimental prototype is constructed, and experimental results are given to verify the effectiveness of the proposed wireless USM. Promisingly, as the first attempt in an unexplored field of non-magnetic wireless motors, this work confirms that WPT and USM can be perfectly integrated and promotes the development of wireless motors towards the non-magnetic, wireless direct drive, and high-robustness.

REFERENCES

[1] C. C. Mi, G. Buja, S. Y. Choi, and C. T. Rim, "Modern advances in wireless power transfer systems for roadway powered electric vehicles," *IEEE Trans. Ind. Electron*., vol. 63, no. 10, pp. 6533–6545, Oct. 2016.

[2] W. Liu, K. T. Chau, H. Wang, and T. Yang, "Long-range wireless power drive using magnetic extender," *IEEE Trans. Transport. Electrific*., vol. 9, no. 1, pp. 1897–1909, Mar. 2023.

[3] H. Zhang and F. Lu, "An improved design methodology of the double-sided LC-compensated CPT system considering the inductance detuning," *IEEE Trans. Power Electron*., vol. 34, no. 11, pp. 11396–11406, Nov. 2019.

[4] Z. Hua, K. T. Chau, W. Han, W. Liu, and T. W. Ching, "Output-controllable efficiency-optimized wireless power transfer using hybrid modulation," *IEEE Trans. Ind. Electron.*, vol. 69, no. 5, pp. 4627–4636, May 2022.

[5] R. Sedehi et al., "A wireless power method for deeply implanted biomedical devices via capacitively coupled conductive power transfer," *IEEE Trans. Power Electron*., vol. 36, no. 2, pp. 1870–1882, Feb. 2021.

[6] M. Huang, Y. Lu, and R. P. Martins, "A reconfigurable bidirectional wireless power transceiver for battery-to-battery wireless charging," *IEEE Trans. Power Electron*., vol. 34, no. 8, pp. 7745–7753, Aug. 2019.

[7] B. Salvi, S. Porpandiselvi, and N. Vishwanathan, "A three switch resonant inverter for multiple load induction heating applications," *IEEE Trans. Power Electron*., vol. 37, no. 10, pp. 12108–12117, Oct. 2022.

[8] Y. Wang, H. Zhang, and F. Lu, "3.5-kW 94.2% DC–DC efficiency capacitive power transfer with zero reactive power circulating," *IEEE Trans. Power Electron*., vol. 38, no. 2, pp. 1479–1484, Feb. 2023.

[9] Y. Zhang, Z. Shen, W. Pan, H. Wang, Y. Wu, and X. Mao, "Constant current and constant voltage charging of wireless power transfer system based on three-coil structure," *IEEE Trans. Ind. Electron*., vol. 70, no. 1, pp. 1066–1070, Jan. 2023.

[10] W. Han, K. T. Chau, Z. Hua, and H. Pang, "An integrated wireless motor system using laminated magnetic coupler and commutative-resonant control," *IEEE Trans. Ind. Electron*., vol. 69, no. 5, pp. 4342–4352, May 2022.

[11] M. Liu, K. W. Chan, J. Hu, Q. Lin, J. Liu, and W. Xu, "Design and realization of a coreless and magnetless electric motor using magnetic resonant coupling technology," *IEEE Trans. Energy Convers.*, vol. 34, no. 3, pp. 1200–1212, Sept. 2019.

[12] M. Sato, G. Yamamoto, D. Gunji, T. Imura, and H. Fujimoto, "Development of wireless in-wheel motor using magnetic resonance coupling," *IEEE Trans. Power Electron*., vol. 31, no. 7, pp. 5270–5278, Jul. 2016.

[13] C. Jiang, K. T. Chau, C. H. T. Lee, W. Han, W. Liu, and W. H. Lam, "A wireless servo motor drive with bidirectional motion capability," *IEEE Trans. Power Electron*., vol. 34, no. 12, pp. 12001–12010, Mar. 2019.

[14] H. Liu, H. Zhou, Q. Deng, W. Hu, X. Gao, and L. Fang, "A wireless DC motor drive using LCCC-CCL compensated network with bidirectional motion capability," *IEEE Trans. Circuits Syst. I, Reg. Papers*, vol. 69, no. 11, pp. 4714–4725, Nov. 2022.

[15] H. Wang, K. T. Chau, C. H. T. Lee, L. Cao, and W. H. Lam, "Design, analysis, and implementation of wireless shaded-pole induction motors," *IEEE Trans. Ind. Electron*., vol. 68, no. 8, pp. 6493–6503, Aug. 2021.

[16] C. Jiang, K. T. Chau, C. Liu, and W. Han, "Design and analysis of wireless switched reluctance motor drives," *IEEE Trans. Ind. Electron.*, vol. 66, no. 1, pp. 245–254, Jan. 2019.

[17] K. Lu, X. Li, Y. Zhao, P. Yi, B. Yan, and W. Hua, "A novel three-vector-based model predictive flux control with low computation complexity for SPMSM," *IEEE Trans. Transport. Electrific.*, doi: 10.1109/TTE.2023.3315522.

[18] H. Wang, K. T. Chau, C. H. T. Lee, and C. Jiang, "Wireless shaded-pole induction motor with half-bridge inverter and dual-frequency resonant network," *IEEE Trans. Power Electron*, vol. 36, no. 12, pp. 13536–13545, Dec. 2021.

[19] G. A. Covic and J. T. Boys, "Inductive Power Transfer," *Proc. IEEE*, vol. 101, no. 6, pp. 1276-1289, June 2013.

[20] J. Lu, G. Zhu, D. Lin, S. -C. Wong, and J. Jiang, "Load-independent voltage and current transfer characteristics of high-order resonant network in IPT system," *IEEE J. Emerg. Sel. Topics Power Electron*., vol. 7, no. 1, pp. 422-436, Mar. 2019.

[21] J. Dai and D. C. Ludois, "A survey of wireless power transfer and a critical comparison of inductive and capacitive coupling for small gap applications," *IEEE Trans. Power Electron*., vol. 30, no. 11, pp. 6017–6029, Nov. 2015.

[22] Y. Wang, H. Zhang, Y. Cao, and F. Lu, "Remaining opportunities in capacitive power transfer based on duality with inductive power transfer," *IEEE Trans. Transport. Electrific.*, vol. 9, no. 2, pp. 2902-2915, Jun. 2023.

[23] H. Zhang, F. Lu, H. Hofmann, W. Liu, and C. C. Mi, "A four-plate compact capacitive coupler design and LCL-compensated topology for capacitive power transfer in electric vehicle charging application," *IEEE Trans. Power Electron.*, vol. 31, no. 12, pp. 8541–8551, Dec. 2016.

[24] F. Lu, H. Zhang, H. Hofmann, and C. C. Mi, "A double-sided LCLC compensated capacitive power transfer system for electric vehicle charging," *IEEE Trans. Power Electron.*, vol. 30, no. 11, pp. 6011–6014, Nov. 2015.

[25] V. Vu, M. Dahidah, V. Pickert, and V. Phan, "An improved LCL-L compensation topology for capacitive power transfer in electric vehicle charging," *IEEE Access*, vol. 8, pp. 27757–27768, 2020.

[26] L. Pamungkas, S. H. Wu, and H. J. Chiu, "Equivalent circuit approach for output characteristic design of capacitive power transfer," *IEEE Trans. Circuits Syst. II, Exp. Briefs*, vol. 68, no. 7, pp. 2513–2517, Jul. 2021.

[27] F. Lu, H. Zhang, H. Hofmann, and C. C. Mi, "A double-sided LC compensation circuit for loosely coupled capacitive power transfer," *IEEE Trans. Power Electron.*, vol. 33, no. 2, pp. 1633–1643, Feb. 2018.

[28] J. Xia, X. Yuan, S. Lu, J. Li, S. Luo, and S. Li, "A two-stage parameter optimization method for capacitive power transfer systems," *IEEE Trans. Power Electron.*, vol. 37, no. 1, pp. 1102-1117, Jan. 2022.

[29] X. Wei et al., "A circuit design method for constant voltage output with zero phase angle and minimum coupler voltages in capacitive power transfer," *IEEE Trans. Power Electron.*, vol. 38, no. 3, pp. 4181-4192, Mar. 2023.

[30] Z. Wen, X. Li, T. Cao, B. Wang, R. Liu, and D. Wu, "A low-voltage cylindrical travelling wave ultrasonic motor incorporating multilayered piezoelectric ceramics," *IEEE Trans. Ultrason., Ferroelectr., Freq. Control,* vol. 69, no. 6, pp. 2129–2136, Jun. 2022.

[31] S. W. Chung and K. T. Chau, "A new compliance control approach for traveling-wave ultrasonic motors," *IEEE Trans. Ind. Electron*., vol. 55, no. 1, pp. 302–311, Jan. 2008.

[32] H. P. Ko, S. Kim, J. S. Kim, H. J. Kim, and S. J. Yoon, "Wear and dynamic properties of piezoelectric ultrasonic motor with frictional materials coated stator," *Mater. Chem. Phys.*, vol. 90, no. 2, pp. 391–395, Sep. 2005.

[33] X. Yang, D. Zhang, R. Song, C. Yang, and Z. Mu, "Development of a rotary ultrasonic motor with double-sided staggered teeth," *Micromachines*, vol. 12, no. 7, pp. 824, Jul. 2021.

[34] Y. Xiao, Y. Yang, C. Liu, and J. Rodriguez, "Design and analysis of a wireless ultrasonic motor drive system," *IEEE Trans. Power Electron.*, vol. 38, no. 10, pp. 12309–12314, Oct. 2023.

[35] X. Dai, M. Sun, P. Deng, R. Wang, and Y. Su, "Asymmetric bidirectional capacitive power transfer method with push–pull full-bridge hybrid topology," *IEEE Trans. Power Electron.*, vol. 37, no. 11, pp. 13902-13913, Nov. 2022.

[36] X. Qing, Z. Wang, Y. Su, Y. Zhao, and X. Wu, "Parameter design method with constant output voltage characteristic for bilateral LC-compensated CPT system," *IEEE J. Emerg. Sel. Topics Power Electron*., vol. 8, no. 3, pp. 2707–2715, Sept. 2020.

[37] IEEE Standard for Safety Levels with Respect to Human Exposure to Radio Frequency Electromagnetic Fields, 3 kHz to 300 GHz, IEEE Standard C95.1, 2005.

[38] F. Zhang et al., "Hysteresis segmentation modeling and experiment of piezoelectric ceramic actuator," *IEEE Sensors J.*, vol. 22, no. 21, pp. 21153-21162, Nov. 2022.
[39] Z. Yuan, M. Saeedifard, C. Cai, Q. Yang, P. Zhang, and H. Lin, "A misalignment tolerant design for a dual-coupled LCC-S-compensated WPT system with load-independent CC output," *IEEE Trans. Power Electron.*, vol. 37, no. 6, pp. 7480-7492, Jun. 2022.

Zhiwei Xue (Student Member, IEEE) is currently working toward the Ph.D. degree in electrical and electronic engineering with the Department of Electrical and Electronic Engineering at the University of Hong Kong, Hong Kong, China. From 2021 to 2022, he was a Research Assistant at the Department of Electrical Engineering, The Hong Kong Polytechnic University, Hong Kong, China.

His research interests include wireless power transfer, electrical machine drives, power electronics, and electric vehicle technologies.

Kwok Tong Chau (Fellow, IEEE) received the B.Sc. (Eng.), M.Phil., and Ph.D. degrees in electrical and electronic engineering from The University of Hong Kong, Hong Kong, in 1988, 1991, and 1993, respectively. Currently, he serves as Chair Professor of Electrical Energy Engineering at the Research Centre for Electric Vehicles and Department of Electrical and Electronic Engineering, The Hong Kong Polytechnic University. His research interests include electric and hybrid vehicles, power electronics and drives, and renewable energies. He is the author of nine books and more than 350 journal papers.

Prof. Chau is a Fellow of the Institution of Engineering and Technology (IET), U.K., and of the Hong Kong Institution of Engineers. He is also a Co-editor of the Journal of Asian Electric Vehicles. He is a Chartered Engineer. He was the recipient of the Changjiang Chair Professorship from the Ministry of Education, China, and the Environmental Excellence in Transportation Award for Education, Training, and Public Awareness from the Society of Automotive Engineers International.

Wei Liu (Member, IEEE) received the B.Eng. and M.Eng. degrees in electrical engineering from China University of Petroleum, Qingdao, China, and a Ph.D. degree in electrical and electronic engineering from The University of Hong Kong (HKU), Hong Kong, China, in 2014, 2017, and 2021, respectively.

He is currently an Assistant Professor at the Research Centre for Electric Vehicles and Department of Electrical and Electronic Engineering, The Hong Kong Polytechnic University (PolyU). Dr. Liu served as a Postdoctoral Fellow and then was promoted to a Research Assistant Professor from 2021 to 2023, and he is now an Honorary Assistant Professor at the Department of Electrical and Electronic Engineering, HKU. He also worked as a Visiting Researcher with Nanyang Technological University, Singapore (NTU), in 2019. His research interests include wireless power transfer, power electronics, biomedical power electronics, and electric vehicle technologies.

Dr. Liu was the recipient of the Power Engineering Prize from HKU, the Excellent Paper Award, and the Best Presentation Award from international conferences in the area of Electric Vehicles and Transportation Electrification. He is also a Guest Associate Editor of *IEEE Journal of Emerging and Selected Topics in Power Electronics (JESTPE)*, Guest Editor of international journals, and Session Chair of international conferences.

Tze Wood Ching (Senior Member, IEEE) received t he B.Eng. and M.Sc. degrees from the Department of Electrical Engineering, Hong Kong Polytechnic Univ ersity, Hong Kong, and Ph.D. degrees from the Depar tment of Electrical and Electronic Engineering, Unive rsity of Hong Kong, Hong Kong, in 2002. His main re search interests include clean energy, power electroni c converters, electric machines and drives, electric ve hicles and charging infrastructure.

He has had more than ten years of industrial exper ience and worked in Hong Kong Electric Co. and CLP Power (HK) Ltd., Hon g Kong. He served as an Assistant Professor in the Department of Electromec hanical Engineering, at the University of Macau, Macao. He is currently a Lec ture in the Department of Electrical and Electronic Engineering, The Universit y of Hong Kong, Hong Kong.

Dr. Ching is a Senior Member of the IEEE, a Chartered Engineer of the UK,a Member of the Institution of Engineering and Technology (UK), a Member of the Chartered Institution of Building Services Engineers (UK) and a Member of the Hong Kong Institution of Engineers. He served as Special Session Chair of IEEE-IECON12, IEEE-ISIE13, IEEE-ICIT15, IEEE-IEMDC15, IEEE-IECON15, EVER16, IEEE-IEMDC2017 and Intermag-2018.